Temperature Dependence of X- and Q-Band EPR Spectra of the Dinuclear Manganese(II) Complex $[(NO_2Bpmp)Mn_2(\mu\text{-}OAc)_2]^+$: Determination of the Exchange Constant and of the Spin Parameters for the $S = 1$, 2, and 3 Spin States

Sébastien Blanchard,[a, b] Guillaume Blain,[a] Eric Rivière,[a] Martine Nierlich,[c] and Geneviève Blondin*[a]

Abstract: A new dinuclear manganese(II) complex was synthesised with the biscompartimental ligand 2,6-bis[bis(2-pyridylmethyl)aminomethyl]-4-nitrophenol (NO_2BpmpH) and characterised by X-ray crystallography. Magnetic susceptibility measurements revealed that the two high-spin Mn^{II} ions are antiferromagnetically coupled with a singlet-to-triplet separation of 7.2 cm^{-1}. The powder EPR spectra were recorded for both X- and Q-bands between 1.8 K and 35 K. A detailed analysis of these spectra led to the determination of three out of five individual spin-state zero-field splitting parameters. From the proposed simulations, the exchange coupling constant J and the intermetallic distance have been computed.

Keywords: EPR spectroscopy · exchange interactions · manganese · N,O ligands

Introduction

EPR spectroscopy has proved to be a powerful technique for elucidating the electronic structure of active sites in metalloproteins in which paramagnetic ions are embedded. This is particularly true for dinuclear manganese(II)-containing enzymes. Examples of these enzymes are the Mn-based catalases, which promote the dismutation of hydrogen peroxide into water and dioxygen,[1, 2] and arginase, which is responsible for the hydrolysis of L-arginine to L-ornithine and urea.[3] Furthermore, EPR spectroscopy and the electronic properties of Mn^{II} can jointly be used to get new insights into the catalytic cycles of metalloproteins for which the identity of the physiological divalent metal ion cofactors is not yet known.[4]

EPR data gathered on dinuclear Mn^{II} systems are characterised, firstly, by the broad spectral width using an X-band frequency and, secondly, by their strong temperature-dependence.[5] The latter is controlled by the isotropic exchange interaction between the two high-spin Mn^{II} ions ($S_{Mn^{II}} = 5/2$), while the former is related, among other parameters, to the Mn – Mn dipolar coupling. However, both interactions depend intimately on the chemical nature of the bridging ligand(s) and also on the intermetallic Mn ··· Mn separation.[6] Hence, a profound analysis of their EPR spectra gives a unique opportunity to address the chemical nature of the dinuclear Mn^{II} core. This approach has been tentatively followed for the dimanganese cores of the catalase from *Thermus thermophilus* and of the rat liver arginase,[7] for the manganese center of the dinitrogenase reductase-activating glycohydroxylase from *Rhodospirillum rubrum*,[8] and for the reconstruction of the manganese cluster in the apo-water oxidation complex of Photosystem II in green plants.[9]

The analysis of the EPR data reported in previous works[7, 8, 10] relies on the mathematical deconvolution of the temperature-dependent spectra that were recorded at a single microwave frequency, namely 9.4 GHz. The dimanganese(II) units present an antiferromagnetic exchange interaction leading to a diamagnetic ground state and excited paramagnetic states associated with integer spin values ranging from 1 to 5. The convergence criterion of the deconvolution

[a] Dr. G. Blondin, Dr. S. Blanchard, G. Blain, Dr. E. Rivière
Laboratoire de Chimie Inorganique
UMR 8613, LRC-CEA n°33V
Institut de Chimie Moléculaire et des Matériaux d'Orsay
Bâtiment 420, Université Paris-Sud
91405 Orsay Cedex (France)
Fax: (+33) 1-69-154-754
E-mail: gblondin@icmo.u-psud.fr

[b] Dr. S. Blanchard
Current address:
Max-Plank-Institut für Strahlenchemie, Stiftstrasse 34 – 36,
45470 Mülheim an der Ruhr (Germany)

[c] M. Nierlich
DRECAM/SCM Bat 125, CEA Saclay
91191 Gif-sur-Yvette (France)

Supporting information for this article is available on the WWW under http://www.chemeurj.org, or from the author.

DOI: 10.1002/chem.200304759

procedure is the temperature-dependent contributions of the $S=1$ and $S=2$ spin states that must obey the Boltzmann law. This leads to the determination of the strength of the exchange coupling and to the temperature-independent triplet- and quintet-spin-state spectra. No simulation of the extracted individual spin-state EPR traces are presented and only one spin parameter value (D_2) is proposed based on the position of the highest field line. The lack of a precise analysis of the individual spin-state EPR spectrum profiles calls into question the validity of the results obtained by using a deconvolution process. Actually, the magnitudes of the exchange interactions between the two Mn^{II} ions in the manganese catalases have been deduced from the variation with temperature of the magnetisation, and were found to be two, or even four, times weaker than that suggested from EPR measurements.[6, 11]

We have recently reported a detailed investigation of the EPR properties of the antiferromagnetically coupled dinuclear manganese(II) complex $[Mn_2(Bpmp)(\mu\text{-}OAc)_2](ClO_4)\cdot(C_2H_5)_2O$ (**1**) (BpmpH = 2,6-bis[bis(2-pyridylmethyl)aminomethyl]-4-methylphenol).[5] In that work, we reported a new methodology that relies purely on a careful examination of the recorded EPR spectra. We showed therein how the concomitant use of two recording frequencies enabled us to underpin the attribution of the spin parameters of the two first excited spin states ($S=1$ and $S=2$). In addition, we were successful in determining the Heisenberg exchange coupling constant J from the temperature dependence of the EPR spectra. The obtained J value was found to be in good agreement with the one deduced from the magnetisation measurements. This was the first time that such an agreement was reached.

In this paper, we report a more refined analysis on the closely related complex $[Mn_2(NO_2Bpmp)(\mu\text{-}OAc)_2](ClO_4)\cdot 1.5\,CH_3CN\cdot 0.5\,CH_3OH$ (**2**), whereby NO_2BpmpH stands for the ligand 2,6-bis[bis(2-pyridylmethyl)aminomethyl]-4-nitrophenol. The X-ray structure has been solved and magnetisation measurements have revealed a weaker antiferromagnetic exchange interaction relative to that of **1**. In this work, not only the $S=1$ and $S=2$ spin parameters, but also those of the $S=3$ spin state, are retrieved with our methodology. Simulations of the X- and Q-band spectra up to 35 K allow the calculation of the coupling constant (J), and the obtained value is fully consistent with the magnetisation data. Furthermore, from the proposed spin parameters, we are able to attain an intermetallic distance that is in the same range as that observed in **2** by X-ray diffraction.

Results

The dinuclear Mn^{II} complex was synthesised according to the procedure previously reported for **1**,[5] with slight modifications due to the withdrawing effects of the *para*-nitro function (see Experimental Section). X-ray quality crystals of general formula $[Mn_2(NO_2Bpmp)(\mu\text{-}OAc)_2](ClO_4)\cdot 2\,CH_3CN$ were obtained from slow diffusion at room temperature of diethyl ether into a saturated acetonitrile solution of the isolated powder of **2**.

X-ray structure: The structure of the dinuclear complex $[Mn_2(NO_2Bpmp)(\mu\text{-}OAc)_2]^+$ is shown in Figure 1. Manganese–ligand bond lengths and the principal features of the μ-phenoxo-bis(μ-acetato)dimanganese(II) core structure are listed in Table 1. The two manganese ions are hexacoordinate

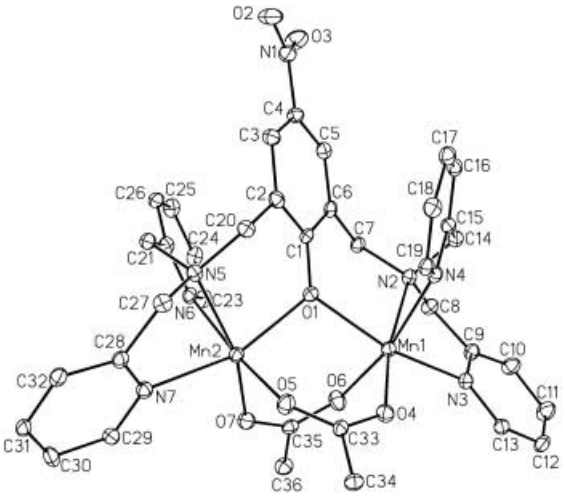

Figure 1. ORTEP view of the X-ray structure of the dinuclear complex $[(NO_2Bpmp)Mn_2(\mu\text{-}OAc)_2]^+$.

Table 1. Metal–ligand principal bond lengths [Å] and angle [°] of the di-Mn^{II}(μ-phenoxo)(di-μ-acetato) core structure of **2**.

Mn1–O1	2.162(4)	Mn2–O1	2.147(4)
Mn1–O4	2.112(4)	Mn2–O5	2.142(4)
Mn1–O6	2.107(4)	Mn2–O7	2.077(4)
Mn1–N2	2.321(5)	Mn2–N5	2.337(5)
Mn1–N3	2.283(5)	Mn2–N6	2.292(5)
Mn1–N4	2.286(5)	Mn2–N7	2.253(5)
Mn1···Mn2	3.450(3)	C1–O1	1.316(6)
Mn1-O1-Mn2	106.41(16)		

in an N_3O_3 distorted octahedral environment. The Mn–O and Mn–N bond lengths fall in the usual range observed for Mn^{II} complexes, with the $Mn–N_{amine}$ distances being slightly longer than the $Mn–N_{pyridine}$ ones. The Mn2 ion has two different $Mn–O_{acetato}$ (2.142(4) and 2.077(4) Å) and $Mn–N_{pyridine}$ (2.292(5) and 2.253(5) Å) distances, like the two Mn^{II} ions in $[Mn_2(Bpmp)(\mu\text{-}OAc)_2]^+$. On the other hand, the coordination sphere of the Mn1 site is more regular: the two $Mn–O_{acetato}$ distances are almost identical (2.112(4) and 2.107(4) Å), as are the two $Mn–N_{pyridine}$ separations (2.283(4) and 2.286(4) Å). The substitution of the methyl group in the $Bpmp^-$ ligand by the withdrawing nitro function has important consequences on the structural features of the bridging phenolate. The Mn–O distances in **2** are elongated relative to those in **1** (2.162(4) and 2.142(4) Å vs 2.103(3) and 2.117(3) Å). This lengthening of the bridging bond lengths is directly related to the decrease in the electronic density on the bridging phenolic oxygen due to the withdrawing effect of the nitro group. This is indeed confirmed by the shortening of the C1–O1 bond (1.316(6) Å in **2** vs 1.339(6) Å in **1**), so that it now exhibits significant double bond character. This modification in the Mn-O-Mn motif leads to a greater separation of

the two metallic sites in $[Mn_2(NO_2Bpmp)(\mu\text{-}OAc)_2]^+$ than in $[Mn_2(Bpmp)(\mu\text{-}OAc)_2]^+$: 3.450(3) Å versus 3.412(1) Å.

Magnetic properties: The variation of the molar magnetic susceptibility with temperature reveals, as expected, an antiferromagnetic interaction between the two high-spin Mn^{II} ions ($S_A = S_B = 5/2$). The main characteristics are the decrease, with decreasing temperature, of the $\chi_M T$ product (from 7.99 $cm^3 mol^{-1} K$ at 294 K to 0.015 $cm^3 mol^{-1} K$ at 2 K), and the maximum of the χ_M versus T curve at 28 K ($\chi_M = 0.090\ cm^3 mol^{-1}$) (see Figure S1 in the Supporting Information). The best fit of the experimental data was obtained by using the van Vleck formula with $g = 2.01$ and $J = 7.2\ cm^{-1}$ ($H = J\hat{S_A}\hat{S_B}$).[12] The spin ladder is thus organised with a $S = 0$ diamagnetic ground state and $S = 1-5$ excited spin states lying at J, $3J$, $6J$, $10J$ and $15J$, respectively, whereby the energies obey the Landé interval rule. It is interesting to note that the introduction of the nitro group at the *para* position of the phenol ring induces a significant drop of the J constant (9.6 cm^{-1} in **1**). This originates from the withdrawing properties of the *para*-nitro function, which weakens the $Mn-O_{phenoxo}$ bonds (see above). A recently published correlation between the exchange coupling constant J and the average bond length between the manganese(II) ions and the bridging phenolic oxygen in $[Mn^{II}(\mu\text{-phenoxo})(\mu\text{-acetato})_2Mn^{II}]^+$ systems clearly indicates the decrease of J with increasing Mn–O distance.[13] Indeed, the point corresponding to the $[(NO_2Bpmp)Mn_2(\mu\text{-}OAc)_2]^+$ complex matches the proposed correlation line.

The dinuclear nature of **2** is maintained upon dissolution, as indicated by the EPR spectra recorded on frozen solutions at 9.4 GHz and 34 GHz (Figure 2). In the X-band spectra, eleven hyperfine lines are clearly detected between 235 and 280 mT, with an average spacing of 4.42 mT. Another set of lower intensity lines starting at 284 mT is also observed, with a 4.5 mT average separation (see insert in Figure 2). Less resolved hyperfine lines are also observed between 80 and 115 mT, as well as between 370 and 420 mT, for which a separation of 4.4 mT can be estimated. Similar features have been previously observed in dinuclear Mn^{II} systems.[5, 7, 13–22] In the Q-band spectra, thirty-three hyperfine lines, regularly spaced by 4.5 mT, are clearly in evidence between 1156 and 1301 mT. In addition, the first ten and the last seven lines satisfy the 1:2:3:4:5:6:5:4:3:2:1 intensity profile. Such spectroscopic features are expected for the interaction between the electronic spin and two equivalent Mn nuclear spins ($I_{Mn} = 5/2$),[23] therefore attesting to the dinuclear Mn^{II} core structure of compound **2** in solution.

Powder EPR spectra: Experimental X- and Q-band EPR spectra recorded on powder samples are reported in Figures 3 and 4 together with their simulations (see below). Even after successive recrystallisation, a contaminating mononuclear Mn^{II} impurity was detected and was clearly identified by the six-line signal around $g = 2$ (337 mT for X-band, 1218 mT for Q-band) exhibiting a peak-to-trough separation of 55 mT at both frequencies. This signal decreases in intensity as the temperature is increased, as expected from the Curie law associated with an isolated $S = 5/2$ system. Therefore, excluding the Mn^{II} impurity extra signal, the spectra presented here are pretty similar to the ones previously reported for **1**. The X-band spectra spread from 0 to 800 mT at low temperature and gain intensity in the $g = 2$ region, to the detriment of the wings, as the temperature is increased. In the Q-band spectrum, the most intense transition is seen around 600 mT at 5 K; raising the temperature leads to a continuous decrease in intensity. In contrast, the $g = 2$ region gains intensity as the temperature is increased. A similar behaviour was observed for the EPR spectra of **1**. Nevertheless, a closer inspection of Figures 3 and 4 reveals important differences between the EPR signatures of **1** and **2**, suggesting that the spin parameters are different for both complexes.

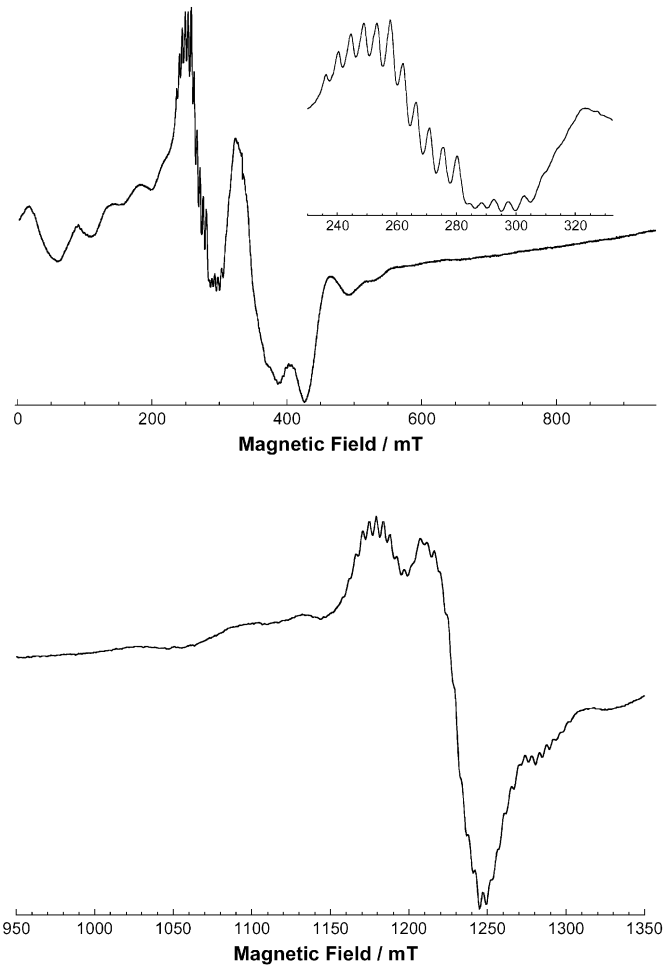

Figure 2. Frozen solution EPR spectra recorded at 9.38 GHz and 20 K (top) and 34 GHz and 80 K (bottom).

Determination of the spin parameters: The methodology used to analyse the EPR spectra has been explicitly presented in reference [5]. It is based on a scrupulous examination of the series of spectra recorded for both X- and Q-bands.

When the exchange coupling is the dominant interaction, the EPR spectra profiles are governed by the zero-field splitting effects within each paramagnetic spin state (S). Equation (1) gives the spin Hamiltonian for each spin state.[24]

$$H_S = \mu_B \hat{B}_0 \tilde{g}_S \hat{S} + D_S\left[\hat{S}_z^2 - \frac{1}{3}S(S+1)\right] + E_S[\hat{S}_x^2 - \hat{S}_y^2] + \sum_{i=A,B} \hat{I}_i \tilde{A}_S^i \hat{S} \qquad (1)$$

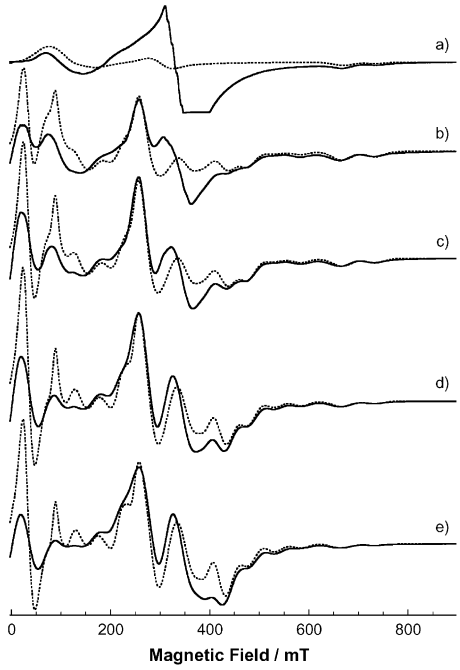

Figure 3. Experimental (continuous line) and simulated (dotted line) X-band spectra at several temperatures: a) 2.5 K, b) 5 K, c) 9 K, d) 14 K and e) 20 K. EPR conditions for spectrum a): 9.4549 GHz microwave frequency, 5.065 mW microwave power, 0.5 mT modulation amplitude, 100 kHz modulation frequency. EPR conditions for spectra b)–e): 9.3915 GHz microwave frequency, 2.007 mW microwave power, 0.5 mT modulation amplitude, 100 kHz modulation frequency. Spectrum a) was scaled approximately to be compared to spectra b)–e). See text for the simulated spectra.

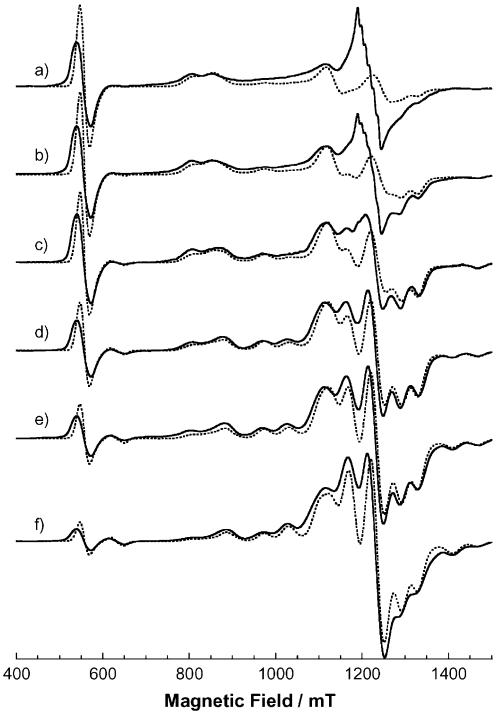

Figure 4. Experimental (continuous line) and simulated (dotted line) Q-band spectra at several temperatures: a) 5 K, b) 7 K, c) 9 K, d) 15 K, e) 20 K and f) 30 K. EPR conditions for spectra a)–f): 34.1 GHz microwave frequency, 2.227 mW microwave power, 0.5 mT modulation amplitude, 100 kHz modulation frequency. The six traces may be directly compared. See text for the simulated spectra.

The first term stands for the Zeeman interaction, the second and third terms for the zero-field splitting effect and the last term for the hyperfine interactions between the electronic spin S with the two Mn nuclear spins ($I_A = I_B = 5/2$). For the sake of simplicity we assume, in the forthcoming analysis, an isotropic Zeeman effect characterised by a g_S factor equal to 2 and we neglect the Mn-hyperfine interactions. Indeed the Mn^{II} ion has a high-spin d^5 electronic configuration that is a half-filled shell, and no Mn-hyperfine interaction was detected in the powder spectra.

Our rational approach to tackling the investigation of the experimental data is now outlined. First, the different transitions are assigned to the S spin levels in order to determine the spin parameters, that is, the D_S and E_S zero-field splitting parameters which control the spin-state signature. The use of two microwave frequencies allows such a determination with strong confidence. In addition, the sign of the D_1 parameter can be determined according to the relative intensities of the EPR transitions detected below 10 K. Indeed, at sufficiently low temperature, they depart from the ratios expected in the high-temperature limit. With increasing temperature, such effects vanish and only temperature-independent individual spin traces are considered. This means that the calculated transition probabilities do not account for temperature effects within each spin level and that the calculated spin spectra do not depend on the sign of the associated D_S parameters. Once the temperature-independent spin spectra are known, the linear combinations that best reproduce the experimental EPR traces are established. The weighted coefficients are then fitted as a function of the temperature and the exchange constant J is extracted. In this framework, the following zero-field splitting parameter values for the $S = 1$ and $S = 2$ spin states were determined for **1**: $D_1 = -0.428\ cm^{-1}$, $E_1/D_1 = 0.150$, $D_2 = -0.110\ cm^{-1}$, $E_2/D_2 = 0.125$.

The 5 K Q-band spectrum of **2** (trace a on Figure 4) shows intense resonances at 555, 806, 854 and 1116 mT and weaker ones at 975, 1290, 1327 and 1464 mT. The most intense lines can be attributed to the S = 1 excited spin state. The half-field transition detected when the zero-field splitting parameter D_1 is lower in absolute value than the recording microwave frequency is located at 555 mT. By comparison with the 34 GHz $S = 1$ signature of **1**, the 806, 854 and 1116 mT lines are assigned as the lowest z, y and x lines, respectively (in **1**, they were observed at 755, 861 and 1056 mT, respectively). Taken together, these values suggest a smaller $|D_1|$ parameter and a stronger rhombicity (i.e., E_1/D_1) for **2** as compared to **1**. This is indeed confirmed by calculation of the triplet spectrum. Using the parameters listed in Table 2, a good simulation of the 5 K Q-band spectrum can be obtained. These $S = 1$ spin parameter values are indeed corroborated by the calculation of the X-band spectrum. As can be seen from trace a of Figure 3, the principal features detected at 2.5 K at 69, 667 and 736 mT are correctly reproduced with the same set of parameters for the $S = 1$ spin state. In addition, these signals decrease in intensity when the temperature is lowered to 1.8 K (see Figure S2 in the supporting information), in agreement with their assignment to the triplet excited spin state.

Table 2. Spin parameters used for the calculation of the $S=1$, 2 and 3 spin state spectra for both X- and Q-bands.

				X-band				Q-band			
S	D_S [cm^{-1}][a]	E_S/D_S[a]	g_{iso}	ω_x [mT][b]	ω_y [mT][b]	ω_z [mT][b]	Sophe grid[c]	ω_x [mT][b]	ω_y [mT][b]	ω_z [mT][b]	Sophe grid[c]
1	−0.377	0.242	2	17.5	22.5	22.5	60 × 30	17.5	22.5	22.5	40 × 10
2	−0.104	0.162	2	20.0	17.5	20.0	40 × 80	17.5	17.5	15.0	40 × 10
3	−0.059	0.075	2	17.5	15.0	15.0	80 × 150	15.0	17.5	17.5	40 × 10

[a] The uncertainties on the D_S and E_S/D_S values are estimated to be ±0.005 cm^{-1} and 0.005. [b] ω_i stands for the half-width at half-height of the gaussian line in the i direction ($i=x, y, z$). [c] Sophe grid gives the numbers of partitions and segments introduced to get a powder EPR spectrum.

A comparison between the 7 K Q-band spectrum and that at 5 K (Figure 4, trace b) indicates that the weak transitions at 975, 1327 and 1464 mT gain in intensity, and a shoulder on the high-field edge of the 854 mT transition is observed. This temperature-dependent behaviour is a telling indication that those lines are transitions within the $S=2$ spin state. The above-mentioned resonance magnetic field values are very close to those reported for **1**, suggesting that the $S=2$ spin parameters are similar in both complexes. This is confirmed by the variation observed upon increasing the temperature for the X-band spectra, wherein the main features of the $S=2$ spin level are observed at 18, 259, 439, 476 and 589 mT (see Figure 3, trace b), values which can be closely compared to those of **1**. Upon a further increase in the temperature, new transitions are detected that may be ascribed to the $S=3$ spin state. In the Q-band spectra, these are observed at 1027, 1163, 1230, 1288 and 1409 mT (see Figure 4, traces c and d). A gain in intensity for the signal around 900 mT is also perceptible. Whereas in the X-band spectra the main features are seen at 429 and 529 mT (Figure 3, traces c and d), shoulders around 215 and 645 mT can also be observed. From here, the D_S zero-field splitting parameter is estimated by assigning the lowest resonance in the Q-band and the highest in the X-band spectra to z transitions within the spin state. The zero-field splitting rhombicity, that is, the E_S/D_S ratio, is thereafter determined to best reproduce the experimental features.

The associated $S=2$ and $S=3$ spin parameters are listed in Table 2. The temperature-independent spin spectrum does not depend on the sign of the D_S parameter. The negative sign of the D_S parameters proposed here will be discussed below. In our simulations, we have taken different linewidths for X- and Q-band spectra in order to reach the best fits. The origin of this difference may be attributed to different relaxation behaviours at 9.39 GHz and 34.1 GHz. The individual spin spectra are reproduced in Figures 5 and 6. The $g=2$ region is not well reproduced below 10 K for both X- and Q-bands, due to the Mn^{II} impurity. The X-band simulations present a significant discrepancy with the experimental spectra in the 0–200 mT magnetic field domain. This may be attributed to the non-consideration of the Mn-hyperfine interactions, which are competitive with the Zeeman interaction at such low magnetic field strengths.

Spectra recorded at temperatures higher than 25 K are characterised by an increase of the intensity in the $g=2$ region associated with less-defined resonances. The experimental 30 K/9.4 GHz and 35 K/34 GHz spectra are shown in Figure S3 (in the Supporting Information), together with attempts at simulation. The modification of the experimental signatures, and the lack in intensity of the proposed simulations in comparison with the experimental spectra, are due to the appearance of the $S=4$ spin state signal. Unfortunately, for the time being, the absence of defined resonances precludes any precise determination of the corresponding spin parameters.

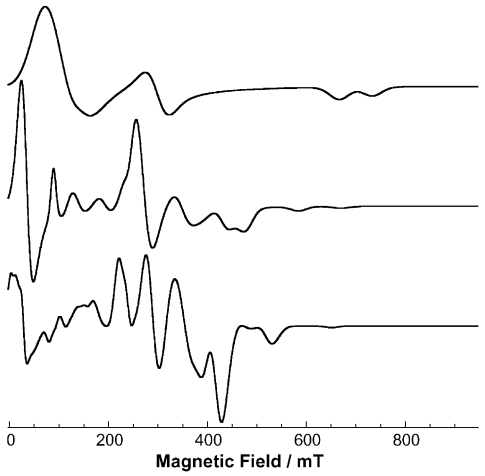

Figure 5. Temperature-independent $S=1$ (upper trace), $S=2$ (middle trace) and $S=3$ (lower trace) spectra calculated at 9.39 GHz. For presentation purposes, the $S=2$ and $S=3$ traces are divided by a factor of 10 and 20, respectively.

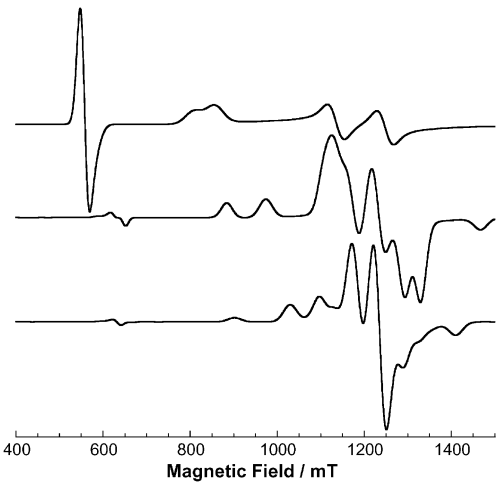

Figure 6. Temperature-independent $S=1$ (upper trace), $S=2$ (middle trace) and $S=3$ (lower trace) spectra calculated at 34.1 GHz. For presentation purposes, the $S=2$ and $S=3$ traces are divided by a factor of 5 and 25, respectively.

D_S sign determination: The proposed $|D_1|$ parameter value is of the same magnitude as the available energy for X- or

Q-band. Consequently, temperature effects of the triplet signature are expected at low temperature. Indeed, the simulation of the spectra recorded at temperatures lower than 10 K may be improved by taking a temperature-dependent trace for the $S=1$ signal. The simulation proposed for the experimental 2.5 K X-band spectrum (trace a of Figure 3) corresponds to the computed 2.5 K $S=1$ spectrum assuming a negative D_1 parameter. At 9.39 GHz, the negative value for a D_1 parameter is responsible for the increase in the ratio of the 667 mT y line intensity over that of the 736 mT z line, when compared to the same ratio evaluated in the high temperature limit (temperature-independent trace). However, at 34 GHz, if a negative sign is considered for D_1, the z line at 806 mT is more intense than the high-temperature limit, relative to the y line at 854 mT. Actually, this is the tendency observed experimentally. However, if a positive D_1 parameter is considered, the reverse situation would be observed for the y versus z transitions. Consequently, this justifies the negative sign proposed for D_1. We also proposed a negative value for the D_2 and D_3 parameters, due to the contribution of the Mn–Mn coupling interaction to the zero-field splitting effect within the higher spin states (see below).

Determination of the exchange coupling constant: The strength of the antiferromagnetic interaction between the two Mn^{II} ions controls the contribution of the spin states to the experimental spectrum recorded at the temperature T. Equations (2) and (3) indicate how the experimental spectra $Y(\nu,B,T)$ are related to the temperature-independent individual spin signatures $Y_S(\nu,B)$:

$$Y(\nu,B,T)=\sum_{S=1}^{5}\frac{n_S(T)}{T}Y_S(\nu,B) \tag{2}$$

$$n_S(T)=\frac{\exp\left[\frac{JS(S+1)}{2k_BT}\right]}{\sum_{S^*=0}^{5}(2S^*+1)\exp\left[\frac{JS^*(S^*+1)}{2k_BT}\right]} \tag{3}$$

In Equation (2), $Y_S(\nu,B)$ stands for the EPR signature of the spin state that would have been obtained on the isolated spin level by using the same recording conditions as those of $Y(\nu,B,T)$. The $n_S(T)$ term reflects the Boltzmann population of the spin level, while the factor $1/T$ reproduces the Curie behaviour of the intensity of the spin spectrum recorded at the temperature T.

Because temperature effects within the spin states disappear above 10 K in both X- and Q-band spectra due to the magnitudes of the zero-field splittings, only temperature-independent spin signatures are considered. For the sake of simplicity, only the simulation of the 2.5 K/9.4 GHz spectrum takes into account temperature effects within the triplet spin level (see above). The other proposed simulations of the experimental EPR spectra $Y(\nu,B,T)$ for both X- ($\nu_X=$ 9.39 GHz) and Q-bands ($\nu_Q=34.1$ GHz) that are shown in Figures 2 and 3, respectively, are obtained according to Equation (4) by using linear combinations of the temperature-independent calculated individual $S=1$ to $S=3$ state spectra $Y_S^{calcd}(\nu,B)$ shown in Figures 5 and 6.

$$Y(\nu,B,T)=\sum_{S=1}^{3}c_S(\nu,T)Y_S^{calcd}(\nu,B) \tag{4}$$

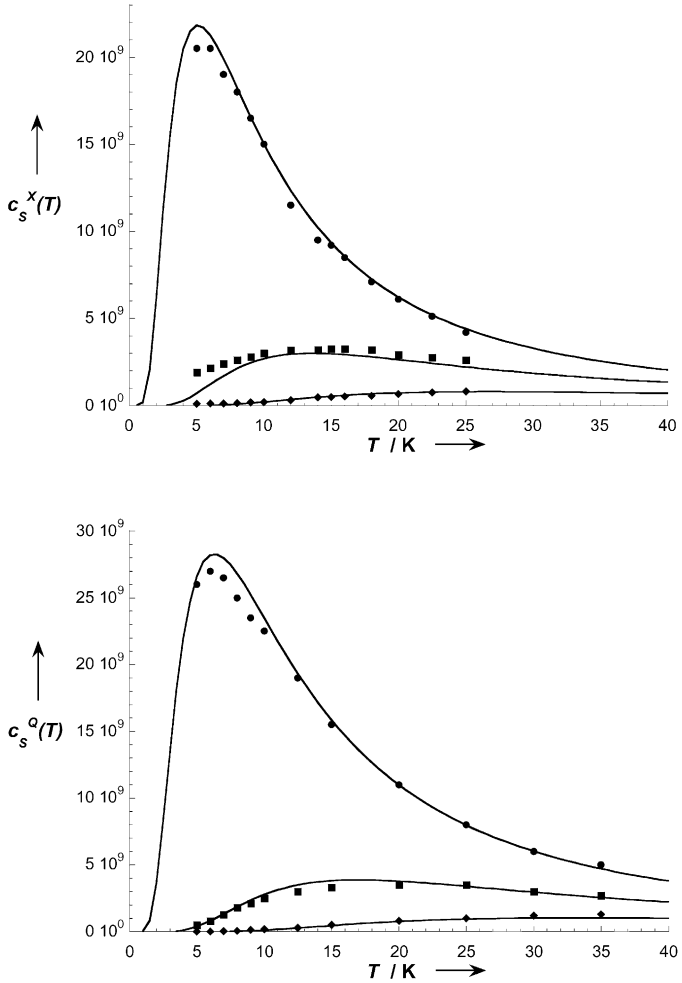

Figure 7. X-band (top) and Q-band (bottom) weighted coefficients for the $S=1$ (●), $S=2$ (■) and $S=3$ (◆) spin states, as a function of temperature. Continuous lines correspond to the best fits with $J=6.0$ cm^{-1} and $\alpha(\nu_X)=$ 95.5 (X-band) and $J=7.4$ cm^{-1} and $\alpha(\nu_Q)=153.6$ (Q-band).

The coefficients $c_S(\nu,T)$ that were used are reported on Figure 7.[25] Comparison of Equation (4) with Equations (2) and (3) leads to the following relation [Eq. (5)]:

$$c_S(\nu T)=\alpha(\nu)\frac{n_S(T)}{T} \tag{5}$$

in which $\alpha(\nu)$ is a scaling factor that depends on the recording conditions (the microwave power, the receiver gain, the modulation amplitude and the quality factor of the cavity). A simultaneous fit of the $S=1$ to $S=3$ weighted coefficients gives $J=6.0$ and 7.4 cm^{-1} for the X- and Q-band data, respectively. The J value obtained from the Q-band data is in good agreement with the value obtained from the magnetic susceptibility measurements ($J=7.2$ cm^{-1}). Although the computed J value from the X-band simulations falls in the same range, we must admit that this difference is far larger than what we expected. The reason for this comes from a sample temperature measurement in our X-band cryostat which is currently less accurate than that in the Q-band cryostat. For instance, an arbitrary increase of all the temperature values by 1 K for the fitting of the X-band weighted

coefficients leads to an exchange coupling constant of 6.5 instead of 6.0 cm^{-1}.

Discussion

Detailed analysis of the EPR spectra of dinuclear Mn^{II} is a critical problem due to the superimposition of several spin state signatures. When the exchange coupling constant J is too small, spectra recorded at 4 K do not originate from a single spin state. Consequently, the determination of the individual spin state spectra is quite difficult. To solve this problem, deconvolution processes[7, 8, 10] have been developed with the main intention of deducing the J constant. There is no doubt that this mathematical approach holds for simultaneously obtaining the individual temperature-independent spin state spectra together with the J constant. However, it is essential to verify the physical significance of all the extracted data in order to validate the proposed results. The principal criticism that one can formulate against these works is the lack of analysis of the individual spin signatures that are obtained following this approach.

We have recently developed a new methodology that relies solely on a rigorous examination of the recorded EPR spectra.[5] The EPR spectra that have been recorded on powder samples of compound **2** show an important contribution of a monomeric Mn^{II} impurity. Its signal spreads on a magnetic field range almost as large as the one of the signal to be analysed precluding the safe application of any deconvolution process. The approach developed herein allows us to leave aside the contaminating signal. Hence, the zero-field splitting parameters and, consequently, the temperature-independent individual spin spectra can still be determined with good accuracy. The exchange coupling constant J is also determined from the series of simulated spectra and the values obtained fall within $\pm 15\,\%$ of the value deduced from magnetic susceptibility measurements. A precise knowledge of the sample temperature, as in the case of Q-band data, leads to a computed J value within an error margin of less than 5 %.

In comparison with our previous work on the complex $[(Bpmp)Mn_2(\mu\text{-}OAc)_2]^+$, for which the spin parameters have been determined for the $S=1$ and $S=2$ states, three spin states ($S=1$, 2 and 3) are fully characterised here. This has allowed access to the Mn–Mn coupling interaction. Indeed, the zero-field splitting effect within the spin states originates from the local zero-field splitting effect on each Mn^{II} center (tensors $\tilde{D}_A$ and $\tilde{D}_B$) and from the coupling interaction between the two paramagnetic sites (tensor $\tilde{D}_{AB}$) according to Equation (6).[24]

$$\tilde{D}_S = d_A(S)\tilde{D}_A + d_B(S)\tilde{D}_B + d_{AB}(S)\tilde{D}_{AB} \quad (6)$$

The tensor $\tilde{D}_{AB}$ includes both the dipolar coupling and the anisotropic component of the exchange interaction. The numerical values of the coefficients are listed in Table 3.[24]

The traceless zero-field splitting tensors are fully characterised by two out of three principal values and by three Euler angles that connect the principal directions to a fixed molecular-based axis system. Since we are investigating a powder, only the eigenvalues of the $\tilde{D}_S$ tensors can be determined. The orientation of the principal directions of the zero-field splitting towards the molecule are not known and may depend on the individual spin level considered. In other words, this means that the $\tilde{D}_S$ tensors are not necessarily collinear. This renders any correlation between the zero-field splitting parameters and structural features more difficult. However, as is shown below, approximations may be formulated that allow a reasonable estimation of the Mn···Mn separation.

Table 3. Numerical values for the $d_A(S)$, $d_B(S)$ and $d_{AB}(S)$ coefficients of Equation (6) for a two $S_i = 5/2$ (i = A, B) coupled system.

S	1	2	3	4	5
$d_A(S) = d_B(S)$	$-16/5$	$-10/21$	$-1/45$	$1/7$	$2/9$
$d_{AB}(S)$	$37/10$	$41/42$	$47/90$	$5/14$	$5/18$

Since we are dealing with a homovalent dimetallic system, only the tensors $\tilde{D}_{cryst} = \tilde{D}_A + \tilde{D}_B$ and $\tilde{D}_{AB}$ are relevant in Equation (6). It can be seen from Table 3 that the lowest contribution of $\tilde{D}_{cryst}$ to the global tensor $\tilde{D}_S$ occurs for the $S=3$ spin state and that the coefficient is much weaker than that of $\tilde{D}_{AB}$ (0.022 vs 0.522). Consequently, we may neglect the contribution of the local zero-field splitting effects to the $\tilde{D}_3$ tensor. Within this hypothesis, $\tilde{D}_3$ depends only on the $\tilde{D}_{AB}$ coupling tensor. Moreover, this spin level presents, among the three characterised in this work, the lowest rhombicity. Therefore we can reasonably consider that the main contribution to the coupling tensor $\tilde{D}_{AB}$ comes from the dipolar coupling, which is characterised by an axial tensor with principal values $-D_{dip}/3$, $-D_{dip}/3$ and $2D_{dip}/3$. Within this framework, the negative sign proposed for D_3 is fully consistent. Along this line, assuming that the $S=3$ tensor $\tilde{D}_3$ originates only from the dipolar coupling, an Mn···Mn separation of 3.58 Å can be estimated from the analytical expression of the D_{dip} parameter [Eq. (7)]:

$$D_{dip} = \frac{3\mu_0\mu_B^2 g^2}{4\pi r^3} \quad (7)$$

This intermetallic distance found is in good agreement with the X-ray crystallographic data of complex **2**, for which a separation of 3.450(3) Å was measured. The 0.13 Å difference found here originates from the successive approximations formulated above. Indeed, the zero-field splitting tensor $\tilde{D}_3$ is not of axial symmetry and the Mn^{II} ions in **2** are not in a regular octahedral environment; this leads to small, local zero-field splitting effects.

Khangulov et al. have previously published a correlation between the D_2 zero-field splitting parameter and the Mn–Mn separation.[7] It must be underlined that the proposed correlation line is established according to the intermetal distances determined from X-ray diffraction studies. Therefore the Mn–Mn separations are not directly deduced from the EPR measurements. Within the hypotheses formulated above, a linear dependence of the D_3 zero-field splitting parameter upon the Mn–Mn distance is also expected. We are currently investigating other dimanganese(II) systems to establish such a correlation.

Furthermore, the D_S-parameter values ($S=1$, 2 and 3) indicated in Table 2 are both in strength and sign entirely compatible with a main contribution of the dipolar coupling to the zero-field splitting effect within each spin level. Indeed, if one assumes that $\tilde{D}_S = d_{AB}(S)\tilde{D}_{AB}$, D_1 and D_2 axial parameter values of -0.418 and -0.110 cm^{-1}, respectively, are calculated from that of D_3 (-0.059). It is worth noticing, firstly, that the values closely match the $|D_S|$ determined from the experimental EPR spectra, and secondly, that the experimentally demonstrated negative sign of D_1 is achieved. This justifies a posteriori the above formulated hypothesis concerning the small amplitude of the local zero-field splitting effects.

Conclusion

We have applied in this paper the methodology recently developed in our lab to investigate the EPR signature of a new dinuclear Mn^{II} complex. The spin parameters for the first three excited spin states, namely $S=1$ to $S=3$, were determined. Linear combinations of individual temperature-independent spin state EPR spectra allowed a good simulation of both the X- and Q-band experimental EPR spectra in a large temperature range. From these simulations, the exchange constant J, together with the $Mn\cdots Mn$ distance, were determined, and the results are fully consistent with those obtained from magnetisation measurements and X-ray diffraction techniques. This sweeps away any doubt about the validity of the spin parameters proposed for the S-spin states.

The methodology that we have developed to analyse the EPR signatures of dimanganese(II) complexes, can be applied to any system that presents spin levels sufficiently separated compared to the EPR microwave energetic quantum. Exchange interaction parameters and structural features may be deduced solely from EPR data. Chemists and biochemists will find here an elaborate new tool for getting new insights into unknown polymetallic cores.

Experimental Section

Reagents and solvents were purchased commercially and used as received.

Caution: Perchlorate salts of metal complexes with organic ligands are potentially explosive. Only small quantities of these compounds should be prepared and they should be handled behind suitable protective shields.

$[Mn_2(NO_2Bpmp)(\mu\text{-}OAc)_2](ClO_4)\cdot 1.5\,CH_3CN\cdot 0.5\,CH_3OH$ (2): The NO_2BpmpH ligand[26] (324 mg, 0.58 mmol) was mixed with $Mn(OAc)_2\cdot 4H_2O$ (282 mg, 1.16 mmol) in methanol (8 mL) for half an hour. Slow addition of a slight excess of $NaClO_4$ (141 mg, 1.16 mmol) dissolved in water (0.5 mL) allowed the precipitation of an orange powder, which was collected by filtration, dissolved in acetonitrile and further recrystallised by slow diffusion of diethyl ether. Elemental analysis calcd (%) for $C_{39.5}H_{42.5}N_{8.5}O_{11.5}ClMn_2$ (965.64): C 49.13, H 4.44, N 12.33, Cl 3.67, Mn 11.38; found: C 48.85, H 4.32, N 12.31, Cl 3.77, Mn 11.10; IR: $\tilde{\nu}=3070$ (w), 2924 (w), 2892 (w), 2835 (w), 1592 (s), 1571 (s), 1506 (m), 1472 (m), 1440 (s), 1430 (s), 1392 (m), 1366 (w), 1317 (s), 1296 (s), 1262 (w), 1154 (w), 1108 (s), 1089 (s), 1048 (m), 1016 (m), 974 (w), 957 (w), 919 (w), 903 (w), 883 (w), 828 (w), 766 (m), 754 (m), 733 (w), 681 (w), 653 (m), 646 (m), 624 (m), 548 (w), 529 (w), 500 (w), 481 (w), 459 (w), 414 (w).

Crystallographic data collection and refinement of the structure of $[(NO_2Bpmp)Mn_2(\mu\text{-}OAc)_2](ClO_4)\cdot 2\,CH_3CN$: A yellow crystal of approximate dimensions of $0.15\times 0.10\times 0.10$ mm was selected. Diffraction collection was carried out on a Nonius diffractometer equipped with a CCD detector. The lattice parameters were determined from ten images recorded with 2° Φ scans and later refined on all data. The data was recorded at 123 K. A 180° Φ range was scanned, with 2° steps, with a crystal-to-detector distance fixed at 30 mm. Data were corrected for Lorentz polarization. The structure was solved by direct methods and refined by full-matrix least-squares on F^2 with anisotropic thermal parameters for all non-H atoms. H atoms were introduced at calculated positions (except for atoms of the solvent molecules) and constrained to ride on their parent C atoms. All calculations were performed on an O2 Silicon Graphics Station with the SHELXTL package.[27]

Formula: $Mn_2C_{40}H_{42}ClN_9O_{11}$; $M_r=970.16$, $T=123(2)$ K, $\lambda=0.71073$ Å; crystallographic system: triclinic; space group: $P\bar{1}$; $a=10.040(2)$, $b=13.594(3)$, $c=16.609(3)$ Å, $\alpha=91.02(3)^\circ$, $\beta=94.88(3)^\circ$, $\gamma=109.71(3)^\circ$, $V=2123.6(7)$ Å^3, $Z=2$, $\rho=1.517$ g cm^{-3}, $\mu=0.729$ mm^{-1}, $\theta_{max}=24.74^\circ$; hkl ranges: $0\le h\le 11$, $-15\le k\le 15$, $-19\le l\le 19$; reflections measured: 13226; independent reflections: 6674; reflections observed with $I>2\sigma(I)$:4326; parameters: 568; $R1=0.0600$ ($R1=\Sigma||F_o|-|F_c||/\Sigma|F_o|$); $wR2=0.1388$ ($wR2=\{\Sigma[w(F_o^2-F_c^2)^2]^2/\Sigma[w(F_o^2)^2]\}^{1/2}$ with $w=1/[\sigma^2(F_o^2)+(0.0744P)^2+1.1323P]$, whereby $P=(F_o^2+2F_c^2)/3$); $(\Delta/\sigma)_{max}=0.025$, $\Delta\rho_{max}=0.427$ e Å^{-3}, $\Delta\rho_{min}=-0.501$.

CCDC 205422 contains the supplementary crystallographic data (excluding structures factors) for this paper. These data can be obtained free of charge via www.ccdc.cam.ac.uk/conts/retreiving.html (or from Cambridge Crystallographic Data Centre, 12 Union Road, Cambridge CB2 1EZ, UK; fax: (+44) 1223-336-033; or e-mail: deposit@ccdc.cam.ac.uk).

Physical measurements: Elemental analyses were performed by the Service de Microanalyse of the CNRS at Gif-sur-Yvette (France) for carbon, nitrogen and hydrogen and by the Service de Microanalyse of the CNRS at Vernaison (France) for manganese and chloride. Infrared spectra were recorded on KBr pellets in the range of 4000–200 cm^{-1} with a Perkin–Elmer Spectrum 1000 spectrophotometer. Magnetic susceptibility data were recorded on a MPMS5 magnetometer (Quantum Design). The calibration was made at 298 K by using a palladium reference sample furnished by Quantum Design. The data were collected over a temperature range of 2–300 K at a magnetic field of 0.1 T and were corrected for diamagnetism. X-band EPR spectra were recorded on a Bruker ELEXSYS 500 (X- and Q-band) spectrometer equipped with an Oxford Instrument continuous-flow liquid-helium cryostat and a temperature control system. The 2.5 K X-band spectrum was recorded on a Bruker ESP 300 spectrometer equipped with an Oxford Instrument continuous-flow liquid-helium cryostat and a temperature control system calibrated with RhFe thermoresistance. Solutions spectra were recorded in acetonitrile as solvent with 0.1M of tetrabutylammonium perchlorate. All the simulations were performed using the Xsophe software (4.0 version) developed by the department of Mathematics at the University of Queensland, Brisbane (Australia).

Acknowledgements

We are grateful to Dr. Alain Boussac (Service de Bioénergétique, URA CNRS 2096, CEA Saclay, Gif-sur-Yvette, France) for EPR facilities and helpful discussions. We thank the Conseil Régional de l'Ile de France for its contribution to the acquisition of the Bruker ELEXSYS X- and Q-band EPR spectrometer. The COST D21 European action and the LRC-CEA project are acknowledged for their financial support.

[1] R. M. Fronko, J. E. Penner-Hahn, C. J. Bender, *J. Am. Chem. Soc.* **1988**, *110*, 7554–7555.
[2] S. V. Khangulov, V. V. Barynin, N. V. Voevodskaya, A. I. Grebenko, *Biochim. Biophys. Acta* **1990**, *1020*, 305–310.
[3] R. S. Reczkowski, D. E. Ash, *J. Am. Chem. Soc.* **1992**, *114*, 10992–10994.
[4] F. Rusnak, L. Yu, S. Todorovic, P. Mertz, *Biochemistry* **1999**, *38*, 6943–6952.
[5] S. Blanchard, G. Blondin, E. Rivière, M. Nierlich, J.-J. Girerd, *Inorg. Chem.* **2003**, in press, and references therein.

[6] L. Le Pape, E. Perret, I. Michaud-Soret, J.-M. Latour, *J. Biol. Inorg. Chem.* **2002**, *7*, 445 – 450.
[7] S. V. Khangulov, P. J. Pessiki, V. V. Barynin, D. E. Ash, G. C. Dismukes, *Biochemistry* **1995**, *34*, 2015 – 2025.
[8] B. S. Antharavally, R. R. Poyner, P. W. Ludden, *J. Am. Chem. Soc.* **1998**, *120*, 8897 – 8898.
[9] G. M. Ananyev, G. C. Dismukes, *Biochemistry* **1997**, *36*, 11342 – 11350.
[10] A. E. Meier, M. M. Whittaker, J. W. Whittaker, *Biochemistry* **1996**, *35*, 348 – 360.
[11] L. Jacquamet, I. Michaud-Soret, N. Debaecker-Petit, V. V. Barynin, J.-L. Zimmermann, J.-M. Latour, *Angew. Chem.* **1997**, *109*, 1697 – 1699; *Angew. Chem. Int. Ed. Engl* **1997**, *36*, 1626 – 1628.
[12] Reasonable fits of the molar magnetic susceptibility vs T curve can be obtained with a J constant lying between 7.0 and 7.4 cm^{-1} when the g factor is fixed between 1.98 and 2.02.
[13] L. Dubois, D.-F. Xiang, X.-S. Tan, J. Pécaut, P. Jones, S. Baudron, L. Le Pape, J.-M. Latour, C. Baffer, S. Chardon-Noblat, M.-N. Collomb, A. Deronzier, *Inorg. Chem.* **2003**, *42*, 750 – 760.
[14] B. Mabad, P. Cassoux, J.-P. Tuchagues, D. N. Hendrickson, *Inorg. Chem.* **1986**, *25*, 1420 – 1431.
[15] D. P. Kessissoglou, W. M. Butler, V. L. Pecoraro, *Inorg. Chem.* **1987**, *26*, 495 – 503.
[16] P. Mathur, M. Crowder, G. C. Dismukes, *J. Am. Chem. Soc.* **1987**, *109*, 5227 – 5233.
[17] M. Mikuriya, T. Fujii, S. Kamisawa, Y. Kawasaki, T. Tokii, H. Oshio, *Chem. Lett.* **1990**, 1181 – 1184.
[18] Y. Gultneh, A. Farooq, S. Liu, K. D. Karlin, J. Zubieta, *Inorg. Chem.* **1992**, *31*, 3607 – 3611.
[19] M. Mikuriya, T. Fujii, T. Tokii, A. Kawamori, *Bull. Chem. Soc. Jpn.* **1993**, *66*, 1675 – 1686.
[20] P. J. Pessiki, S. V. Khangulov, D. M. Ho, G. C. Dismukes, *J. Am. Chem. Soc.* **1994**, *116*, 891 – 897.
[21] T. Howard, J. Telser, V. J. Derose, *Inorg. Chem.* **2000**, *39*, 3379 – 3385.
[22] L. Sun, M. K. Raymond, A. Magnuson, D. Legourriérec, M. Tamm, M. Abrahamsson, P. H. Kenéz, J. Mårtensson, G. Stenhagen, L. Hammarström, S. Styring, B. Åkermark, *J. Inorg. Biochem.* **2000**, *78*, 15 – 22.
[23] V. L. Pecoraro, in *Manganese Redox Enzymes* (Ed.: V. L. Pecoraro), VCH, Weinheim, **1992**, pp. 197 – 231.
[24] A. Bencini, D. Gatteschi, *EPR of Exchange Coupled Systems*, Springer, Berlin, **1990**.
[25] The temperature-independent individual spin trace calculated with the Xsophe program sets the most intense line at 10^8. Dividing this theoretical spectrum by the receiver gain value indicated in the output description file allows a direct comparison of the $S=1$ to $S=3$ signatures.
[26] S. Blanchard, G. Blondin, J.-J. Girerd, unpublished results.
[27] G. M. Sheldrick, SHELXTL-97, Program for the Refinement of Crystal Structures, University of Göttingen, Germany, **1997**.

Received: January 24, 2003 [F4759]